Supplementary Information

Grain boundary generation *via* steering $Cu_xP_2O_{x+5}$ precursor composition enhances CO electrolysis

Jiaqi Sang,‡[ab] Tianfu Liu,‡[a] Pengfei Wei,[a] Hefei Li,[a] Conghui Liu,[ac] Yi Wang,[ab] Youwen Rong,[a] Qi Wang,[d] Guoxiong Wang,*[a] Xinhe Bao*[a]

[a] State Key Laboratory of Catalysis, Dalian National Laboratory for Clean Energy, iChEM (Collaborative Innovation Center of Chemistry for Energy Materials), Dalian Institute of Chemical Physics, Chinese Academy of Sciences, Dalian, 116023, China

[b] College of Energy, University of Chinese Academy of Sciences, Beijing, 100049, China

[c] Zhang Dayu School of Chemistry, Dalian University of Technology, Dalian, 116024, China

[d] School of Materials Science and Engineering, Dalian Jiaotong University, Dalian, 116028, China

‡These authors contributed equally to this work.

Corresponding authors. Email: wanggx@dicp.ac.cn; xhbao@dicp.ac.cn

Experimental details

Materials synthesis

Corresponding stoichiometric amount of cupric oxide (CuO, >99%, Aladdin) and ammonium phosphate ($(NH_4)_2HPO_4$, >99%, Sinopharm Chemical Reagent Co., Ltd., China.) were prepared according to the Cu/P ratio in $Cu_xP_2O_{x+5}$ (x=2, 4, and 5) structure, and the total quality of above chemicals remains constant. The mixture and ethanol was ball-milled with zirconia grinding media for 3 hours at a rate of 300 r min^{-1}. Then the precursor was heated to 250 °C for 6 hours for removing ammonia and water. The solid was grounded for 10 minutes to obtain a dark blue powder, and the powder was then heated at 800 °C for another 12 hours with a ramping rate of 3 °C min^{-1}. The final product was light blue powder for $Cu_2P_2O_7$, green powder for $Cu_4P_2O_9$ and $Cu_5P_2O_{10}$. For comparison, CuO mentioned above was grounded for 10 minutes and directly used as catalyst for comparison.

Crystal structure analysis

The crystal structure of $Cu_xP_2O_{x+5}$ was obtained from XRD patterns. The crystal cell atomicity of Cu, P, and O was calculated. Specifically, atoms occupying unit cell vertex share one-eighth of it, atoms occupying unit cell edge share a quarter of it, atoms occupying unit cell face share half of it, and atoms occupying within unit cell share the whole (Figure S2). The ratio of Cu crystal cell atomicity is its proportion to the total number of crystal cell atomicity. The Cu atom density was further obtained by dividing its value by the unit cell volume.

Electrochemical measurements

Gas diffusion layer (GDL) preparation

Carbon paper (Toray TGP-H-060) was coated with 20 wt% of polytetrafluoroethylene (PTFE, 60 wt%, Sigma-Aldrich) by soaking it into PTFE emulsion solution repeatedly. Then the pretreated carbon paper was heated to 350 °C for 2 hours with a ramping rate of 5 °C min^{-1}. Carbon black ink was prepared by adding the carbon black (Vulcan XC-72R) with 40 wt% PTFE in ethanol, and the ink was painted on one side of the pretreated carbon paper and after that, heated to 350 °C for 2 hours with a ramping rate of 5 °C min^{-1}, thus a gas diffusion layer (GDL) was obtained. The

GDL was regularized into a size of 2 cm×2 cm for electrode preparation.

Gas diffusion electrode (GDE) preparation

Appropriate amount of as-synthesized catalyst was dispersed in ethanol and ultrasonicated for 30 minutes to achieve a homogenous ink. PTFE was added as a binder with a content of 25 wt% and stirred for 10 minutes. For stability test, Nafion ionomer solution (5 wt%, Macklin) was used as a binder rather than PTFE. The ink was dropped on the GDL at 80 °C. The GDL before and after dropping was weighed to calculate the actual loading of the catalyst. In this work, the loading amounts of $Cu_5P_2O_{10}$, $Cu_4P_2O_9$, $Cu_2P_2O_7$, and CuO catalysts were all 1.0±0.1 mg cm^{-2} in the gas diffusion electrode (GDE).

CO electrolysis performance measurements

CO electrolysis performance was evaluated in a membrane and electrode assembly (MEA)-based electrolyzer, which was reported by our previous work.[1] The MEA-based electrolyzer was assembled by cathode, anion exchange membrane and anode. The cathode consists of a graphite flow field plate for gas reactant feeding, an Au-coated Cu plate for current collecting and the GDE with catalyst loading for CO electrolysis. The anode was assembled by a Pt-coated Ti flow field plate for electrolyte supplying (0.1 M potassium hydroxide (KOH, >95%, Macklin)) and current collecting, an Ir-black loaded anode foam for oxygen evolution reaction (OER). For anion exchange membrane, a piece of quaternary ammonia poly(N-methyl-piperidine-co-p-terphenyl) (QAPPT) membrane was used.

CO electrolysis performance was evaluated by using chronopotentionmetry in the galvanostatic mode by an Autolab potentiostat/galvanostat (PGSTAT 302N with 10 A booster). 95%CO/5%N_2 as the gas reactant was fed into the cathode at a flow rate of 30 mL min^{-1} (N_2 was used as the internal standard for quantification of gas products). 0.1 M KOH aqueous solution was used as electrolyte, which was fed into the anode at a flow rate of 5 mL min^{-1}.

Products analysis

Quantification of gas products was proceeded by an online gas chromatography (GC)

(Shimaszu, GC-2014ATFSPL and Angilent, GC8860), which were both equipped with a TCD detector for H_2, N_2 and an FID detector for CH_4, C_2H_4. Liquid products were collected with flow-out electrolyte and analyzed by an offline ^1H nuclear magnetic resonance (NMR) spectrometer (Bruker AVANCE III 400 MHz NMR), with sodium 2, 2-dimethyl-2-silapentane-5-sulfonate (DSS, >97%, Macklin) as an internal standard.

The faradaic efficiency of a specific product i was calculated as follows:

$$f_i = \frac{Q_I}{Q_{total}} \times 100 = \frac{N_i \times n_i \times F}{Q_{total}} \times 100 \quad (1)$$

Where,

f_i: the faradaic efficiency of a specific product i, in CO electrolysis, %;

Q_I: the charge used for the formation of a specific product i, C;

Q_{total}: the total charge passed, C;

N_i: the molar amount of a specific product i, mol;

n_i: the number of electrons transferred for the formation of a specific product i, which is 8 for C_2H_4, 8 for C_2H_5OH, 4 for CH_3COOH, and 12 for C_3H_7OH;

F: the faradaic constant, which is 96485 C mol^{-1}.

The energy efficiency a specific product i production was defined as follows:

$$\varepsilon i = \frac{\Delta H_i^0}{\Delta G_i} \times f_i = \frac{n_i \times F \times E^n}{n_i \times F \times E_i} \times f_i = \frac{E^n}{E_i} \times f_i \quad (2)$$

Where,

εi: the energy efficiency for the specific product i, in CO electrolysis, %;

ΔH^0_i: the theoretical enthalpy change of the specific product i, kJ mol^{-1};

ΔG_i: the Gibbs free energy change of the specific product i, kJ mol^{-1};

f_i: the faradaic efficiency of the specific product i;

n_i: the number of electrons transferred for the formation of a specific product i, which is 8 for C_2H_4, 8 for C_2H_5OH, 4 for CH_3COOH, and 12 for C_3H_7OH;

F: the Faradaic constant, which is 96485 C mol^{-1};

E^n: the thermoneutral voltage which is calculated by ΔH_i^0 and listed in Table S9, V;

E_i: the cell voltage, V.

The energy efficiency of the CO electrolysis production reported in this work is the sum of that of each individual product.

H_2O dissociation performance

The H_2O dissociation performance in Figure S40 was conducted after regular CO electrolysis at 1.0 A cm^{-2} in MEA-based electrolyzer by switching CO flow into Ar flow (30 mL min^{-1}). LSV curves was obtained by scanning the applied potential from –1.0 V to –2.5 V at a rate of 10 mV s^{-1}. Chronopotentiometry was conducted right after LSV at various constant applied current densities.

Physicochemical characterizations

X-ray diffraction (XRD) was acquired on PANalytical X'pert PPR diffractometer with a Cu Kα radiation source (λ = 1.5418 Å). Scanning electron microscopy (SEM) images and energy X-ray spectroscopy (EDS) elemental maps were acquired on JSM-7900F Field-Emission SEM with an accelerating voltage of 5 kV. High-resolution transmission electron microscope (HRTEM) images were acquired by JEM-2100 with an accelerating voltage of 200 kV. Contact angle measurements were conducted by a DSA100 Drop Shape Analyzer. A video recorded the process that a water drop formed *via* the syringe and then front advances on the electrodes surface. Then the video was later analyzed for the contact angle. Each test was conducted two or three times to ensure the accuracy. The qualitative measurement of P element in the electrolyte was confirmed by inductively coupled plasma optical emission spectroscopy (ICP-OES, Optima 7300DV, PerkinElmer). The flow-out electrolyte was collected during CO electrolysis at an applied current density of 0.5 A cm^{-2}.

The chemical composition and value states of the as-synthesized catalysts were measured by quasi-*in situ* X-ray photoelectron spectroscopy (XPS, ESCALAB250xi). For quasi-*in situ* X-ray photoelectron spectroscopy measurement, the electrodes of

catalysts were electrolyzed under CO electrolysis condition in a glovebox and directly transferred into the XPS UHV chamber (SPECS spectrometer equipped with an Al Kα X-ray source) without exposure to air.

Operando X-ray absorption spectra (XAS) of $Cu_5P_2O_{10}$ and $Cu_4P_2O_9$ were acquired in the as-prepared state and under CO electrolysis condition of various applied current densities using a homemade cell with MEA configuration in 0.1 M KOH. Cu K-edge (E_0=8979 eV) XAS measurements were performed at the beamline BL14W1 at Shanghai Synchrotron Radiation Facility (SSRF). The data were obtained using fluorescence-yield mode and taking Cu foil as a reference to calibrate the energy scale. The XAS data was processed by baseline-subtracting and normalizing using IFEFFIT package including ATHENA and ARTEMIS.

Operando Raman spectroscopy measurements of $Cu_5P_2O_{10}$, $Cu_4P_2O_9$, $Cu_2P_2O_7$, and CuO electrodes were conducted by Renishaw inVia Raman microscope with 785 nm near-infrared laser using a homemade cell with MEA configuration for characterization. Anode and anion exchange membrane were used as the same as experimental condition of CO electrolysis, and the cathode catalyst was sprayed on the membrane using Nafion ionomer solution as binder. A long focal length objective lens (Leica, 50×) was used for focusing and collecting the incident and scattered laser light. Electrolysis at each current density from 0.05 A cm^{-2} to 1.0 A cm^{-2} was carried out for more than 5 minutes before signal collection.

Electrosorption of hydroxide (OH^-) was conducted by performing cyclic voltammetry (CV) in an H-cell with Ar-saturated 1.0 M KOH aqueous solution. The linear sweep voltammetry was performed between 0.11 and 0.51 V vs. RHE at a scan rate of 10 mV s^{-1}. The electrode was pre-treated in the MEA-based electrolyzer under CO electrolysis condition at a current density of 0.5 A cm^{-2}, and directly transfer into the H-cell.

Electrochemically active surface area (ECSA) was measured by Pb underpotential deposition (UPD) method in an H-cell.[2] Ar-purged 0.1 M $HClO_4$ and 0.001 M $Pb(ClO_4)_2$ was prepared as solution. In cyclic voltammetry measurements, the potential window was from –0.45 to –0.10 V vs. Ag/AgCl, and the scan rate was

10 mV s^{-1}. Pb stripping current peak was integrated from –0.35 to –0.11 V *versus* Ag/AgCl. The peak area was divided by geometric area and scan rate to calculate the Pb stripping charge over the catalyst per square centimeter. The roughness factor was calculated by comparing the Pb stripping charge of each catalyst with the charge of the oxidation of Pb adatoms over a flat Cu foil (329.3 μC cm^{-2}, which was regarded as 1). The electrodes of $Cu_xP_2O_{x+5}$ and CuO catalysts were pre-treated in the MEA-based electrolyzer under CO electrolysis condition at a current density of 0.5 A cm^{-2}, and were directly transferred into the H-cell.

Grain boundary surface density measurements

The grain boundary of $Cu_xP_2O_{x+5}$ catalysts before and after CO electrolysis were measured from SEM and HRTEM images, respectively. The length of grain boundary presented in each SEM/HRTEM image was measured as $L_{GB,}$ μm. The geometric area of nanoparticles presented in each SEM/HRTEM image was measured as A_{NP}, μm^2. The surface density of grain boundary of each SEM/HRTEM image was defined as follows:

$$\text{Surface density of grain boundary} = \frac{L_{GB}}{A_{NP}}$$

The surface density of grain boundary of each SEM/HRTEM image is measured and calculated, which shows as a mean value, and the error bars represent standard error of the mean. The statistical results are made based on fully separate and identical measurements (Table S5, S6, S8).

Computational setup

Density functional theory (DFT) calculations were performed using the Vienna ab initio simulation package (VASP).[3, 4] The Perdew–Burke–Ernzerhof functional (PBE) from Hammer et al. was employed for electron exchange–correlation.[5, 6] The electron-ion interactions were described by projector augmented wave potentials proposed by Blochl and implemented by Kresse.[7, 8] The plane wave basis set with an energy cutoff of 400 eV was used for geometry optimizations. Spin-polarized calculations were conducted using gamma point of K-mesh. For all the calculations, the van der Waals (vdW) contributions were evaluated with a DFT-D2 method.[9] The electronic energy

and forces were converged to within 1×10^{-6} eV and 0.02 eV $Å^{-1}$. The grain boundary model was built with Aimsgb code by Yang et al.[10] The grain boundary model is composed of 88 atoms as shown in Figure S42 a and b. The Cu (111) is composed of 36 copper atoms as shown in Figure S42 c and d. The bottom three layers of the copper model were fixed and the other atoms were permitted to relax. The vertical vacuum slab was set to be at least 15 Å and a K-mesh of 2×2×1 was used for calculations. The adsorption energy of *CO and *H were calculated with equation (3).

$$E_{ads}(M) = E_{total} - E_M - E_{surface} \quad (3)$$

Where E_{total} is the calculated result of the energy of *CO or *H adsorbed on surface, E_M is the energy of an isolated molecule (M), and $E_{surface}$ is the energy of catalyst model. For the dissociation of H_2O, we used equation (4) to calculate the change of energy:

$$E_{dis} = E_{(*H-*OH)} - E_{(*H2O)} \quad (4)$$

Where E_{dis} is the energy change for H_2O dissociation, $E_{(*H-*OH)}$ is the energy of model with dissociated *H and *OH adsorbed on surface, and E_{*H2O} is the energy of model with $*H_2O$ adsorbed on surface. The computational hydrogen electrode (CHE) model proposed by Nørskov et al. was applied to investigate the free energy profile.[11] In CHE method, the relative free energy change is calculated as:

$$\Delta G = \mu[product] - \mu[reactant] - 0.5\mu[H_2(g)] + eU \quad (5)$$

Where μ is the chemical potential and U is the applied electrical potential. Therefore, in the step involving proton-electron transfer, $\Delta G(U) = \Delta G_0(U) + neU$, where U is the potential versus the reversible hydrogen electrode, ΔG_0 is the free energy at U =0 V.

The Gibbs free energy (G) is calculated with Equation (6).

$$G = E_{Total} + ZPE - TS + \int C_p dT \quad (6)$$

Where E_{Total} is the total electronic energy, ZPE, S and $\int C_p dT$ are the zero-point vibrational energy, entropy and heat capacity at 298.15 K and 1 atm, respectively.

The *COCOH formation energy is used to measure the activity towards C−C

coupling reaction on Cu (111) and grain boundary site, because the *COCOH formation energy is reported as an effective descriptor on catalytic activity differences across various catalysts.[12, 13] We also studied the direct *CO–*CO coupling by performing the search for transition state for *COCO formation (Figure S43). Two H_2O molecules were added to mimic the effect of solvent during calculations.[14] A 4×4 Cu (111) model was used to avoid periodic interactions. The climb image nudged elastic band (CI-NEB) method was used to locate initial guess geometries, and dimer method is used to converge to the saddle points. The imaginary frequency is calculated to confirm the transition state. The grain boundary site exhibits a low activation barrier of 0.67 eV, while Cu (111) demonstrates a higher activation barrier of 1.08 eV. This result is consistent with the formation energy of *COCOH intermediate, which also indicates grain boundary site is superior for C–C coupling reaction compared to Cu (111). Moreover, we studied the C–C coupling on Cu (100), Cu (110) surface and corresponding grain boundaries. As shown in Figure S41, the grain boundaries show a lower formation energy of *COCOH compared to Cu surfaces. Specifically, the formation energy is 0.84 eV on Cu (111)-GB, 0.91 eV on Cu (111), 0.66 eV on Cu (100)-GB, 0.78 eV on Cu (100), 0.74 eV on Cu (110)-GB, 1.02 eV on Cu (110), respectively. We also calculate the C−C coupling on Cu (211) step site, and the result is 1.04 eV. We can see that the C−C coupling reaction is significantly easier on grain boundaries.

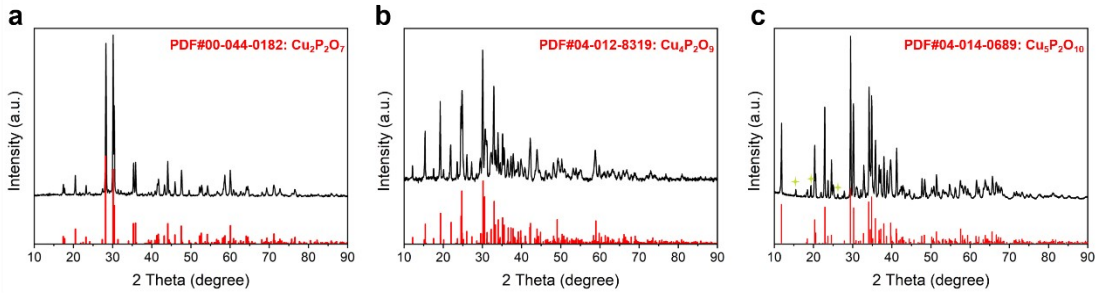

Figure S1. XRD patterns of the as-synthesized (a) $Cu_2P_2O_7$, (b) $Cu_4P_2O_9$ and (c) $Cu_5P_2O_{10}$. The green symbol in (c) ascribes to the feature of $Cu_4P_2O_9$.

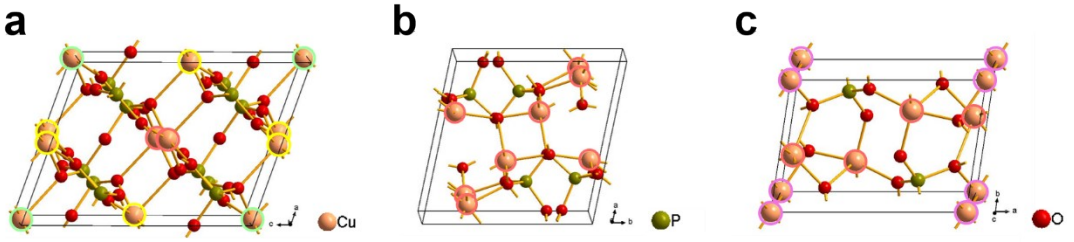

Figure S2. Crystal structure of (a) $Cu_2P_2O_7$, (b) $Cu_4P_2O_9$ and (c) $Cu_5P_2O_{10}$. P atom displays in dark green; O atom displays in red, and Cu atom displays in orange. For distinction, Cu atom occupying unit cell vertex marks in pink purple, Cu atoms occupying unit cell edge marks in green, Cu atoms occupying unit cell face marks in yellow, and Cu atoms occupying within unit cell marks in red.

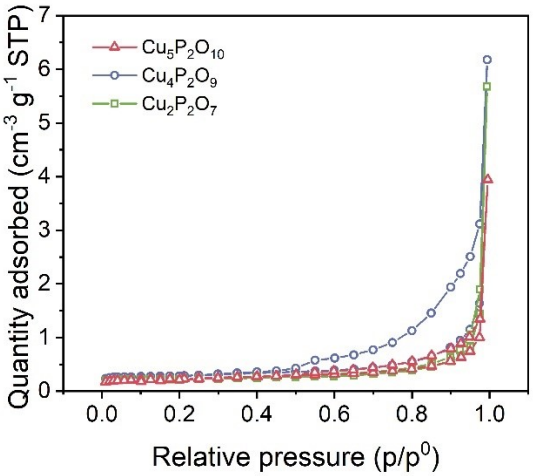

Figure S3. Nitrogen adsorption-desorption isotherms of $Cu_xP_2O_{x+5}$ catalysts before CO electrolysis.

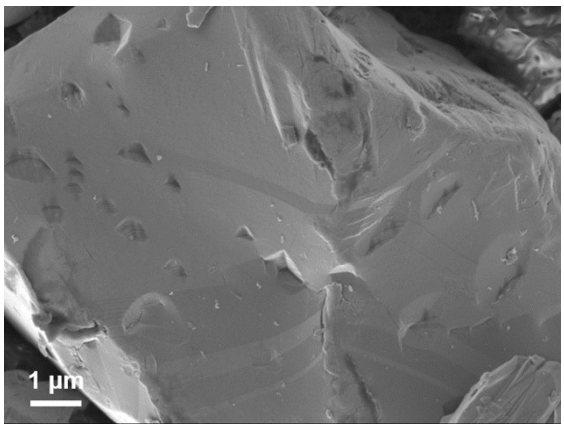

Figure S4. SEM image of the CuO catalyst.

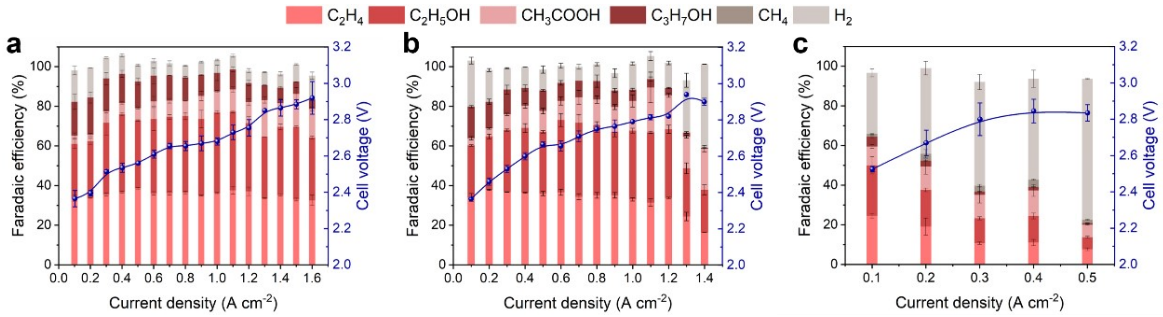

Figure S5. Faradaic efficiencies and current density-cell voltage curves of the reconstructed (a) $Cu_4P_2O_9$, (b) $Cu_2P_2O_7$, and (c) CuO catalysts.

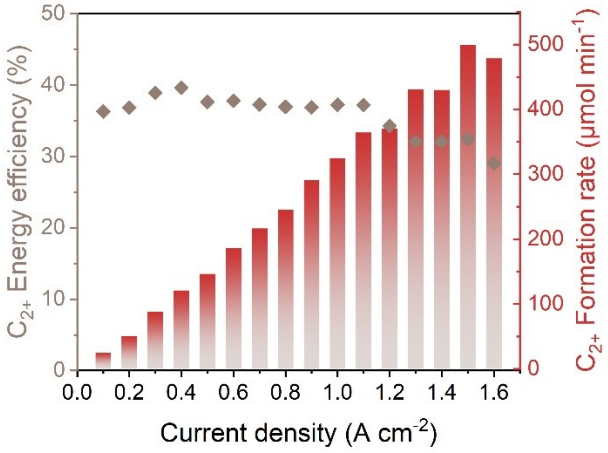

Figure S6. Energy efficiency and formation rate for C_{2+} products over the reconstructed $Cu_4P_2O_9$ catalyst.

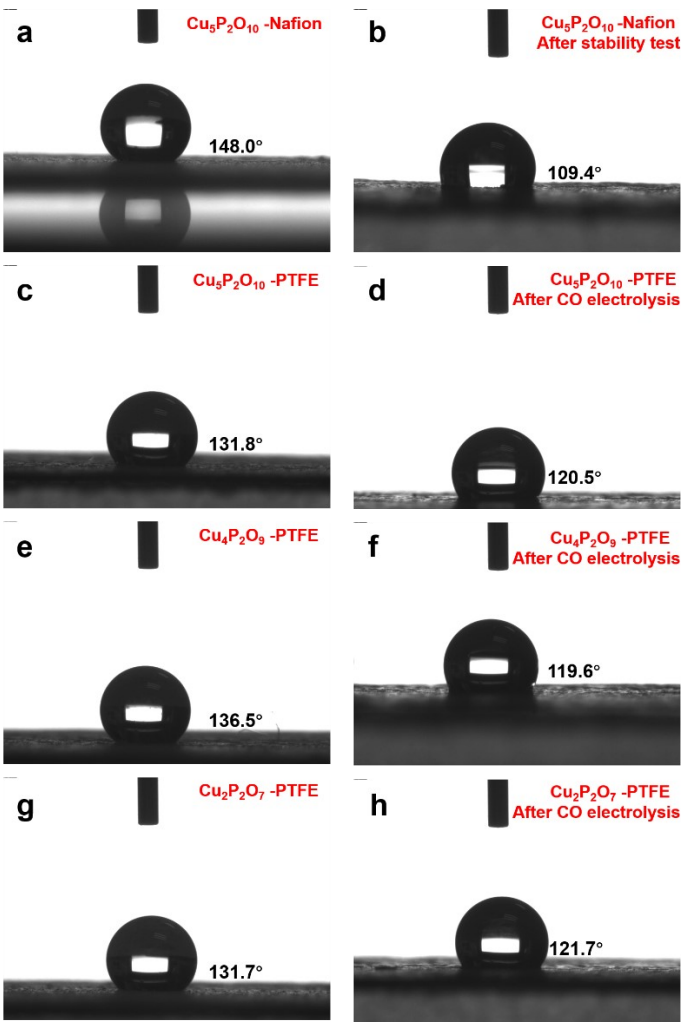

Figure S7. Contact angle measurements of the $Cu_5P_2O_{10}$ electrode with (a), (b) Nafion ionomer and (c), (d) PTFE as the binder before and after stability test and CO electrolysis, respectively. Contact angle measurements of (e), (f) the $Cu_4P_2O_9$ and (g), (h) the $Cu_2P_2O_7$ electrode with PTFE as the binder before and after CO electrolysis.

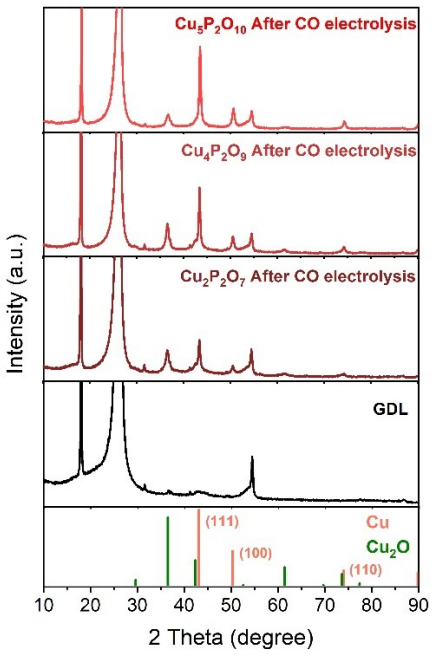

Figure S8. XRD patterns of the reconstructed $Cu_xP_2O_{x+5}$ electrodes after CO electrolysis. The black line ascribes to the feature of GDL.

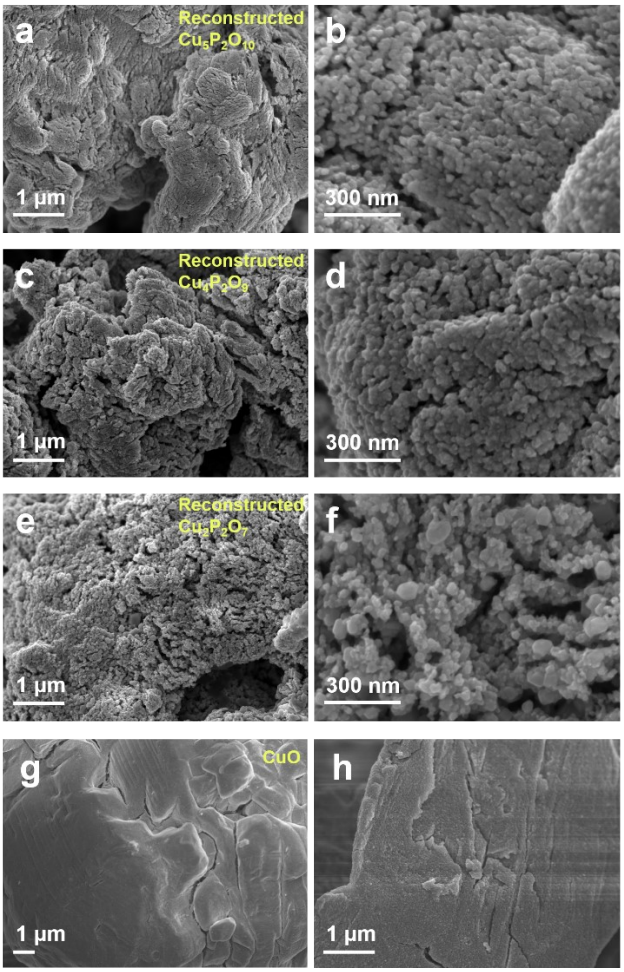

Figure S9. SEM image of the reconstructed (a), (b) $Cu_5P_2O_{10}$, (c), (d) $Cu_4P_2O_9$ and (e), (f) $Cu_2P_2O_7$ and (g), (h) CuO catalysts after CO electrolysis.

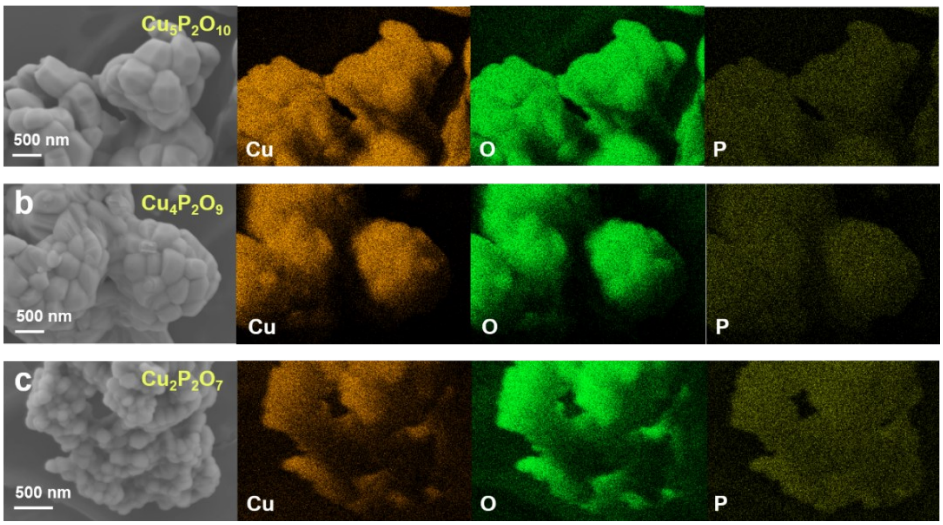

Figure S10. SEM image and EDS elemental maps of the (a) $Cu_5P_2O_{10}$, (b) $Cu_4P_2O_9$ and (c) $Cu_2P_2O_7$ catalysts before CO electrolysis.

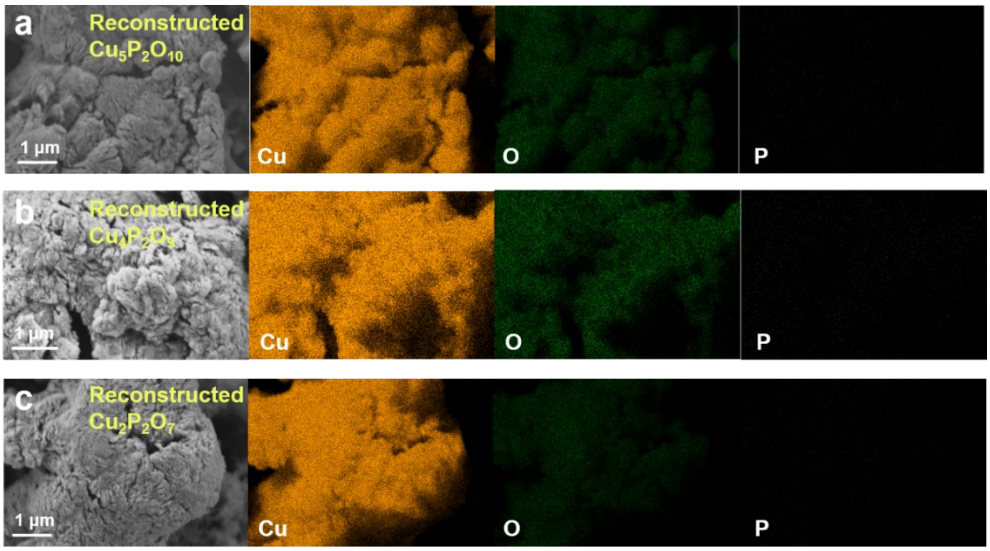

Figure S11. SEM image and EDS elemental maps of the reconstructed (a) $Cu_5P_2O_{10}$, (b) $Cu_4P_2O_9$ and (c) $Cu_2P_2O_7$ catalysts after CO electrolysis.

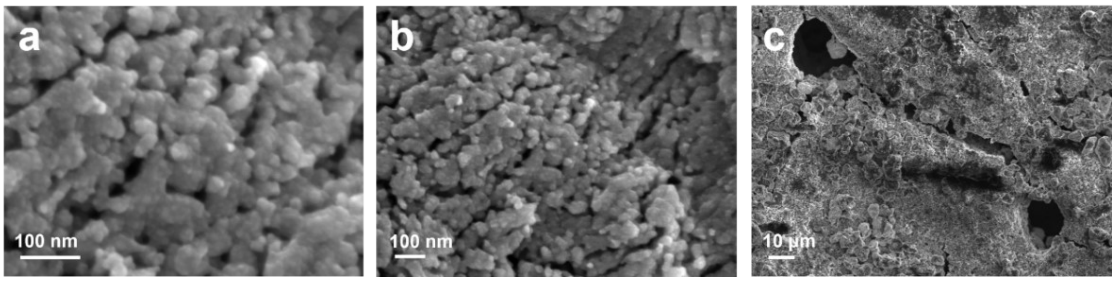

Figure S12. (a) and (b) SEM images of the reconstructed $Cu_5P_2O_{10}$ catalyst after stability test. (c) SEM image of the electrode after stability test.

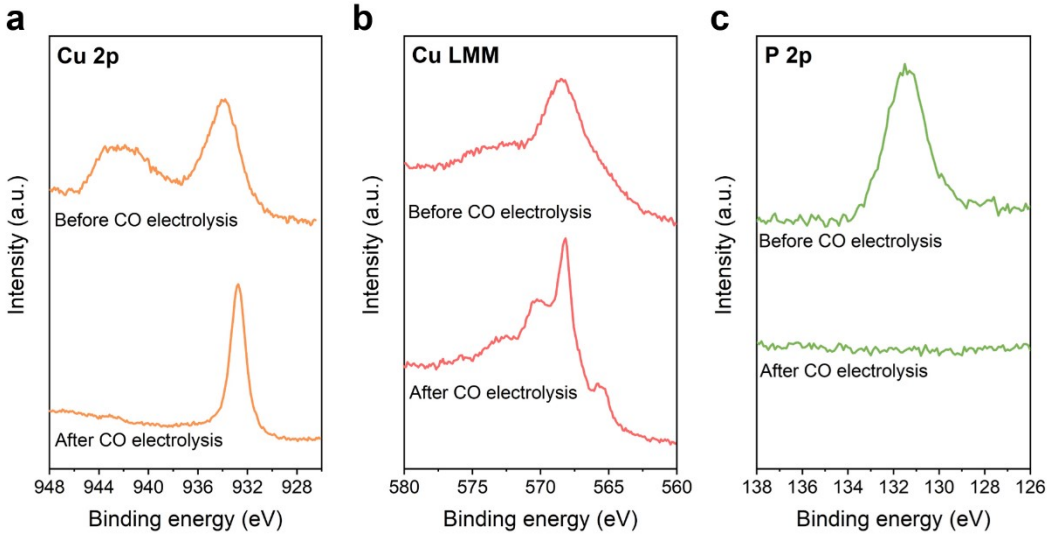

Figure S13. (a) Cu 2p, (b) Cu LMM Auger, and (c) P 2p XPS spectra of the reconstructed $Cu_5P_2O_{10}$ before and after CO electrolysis.

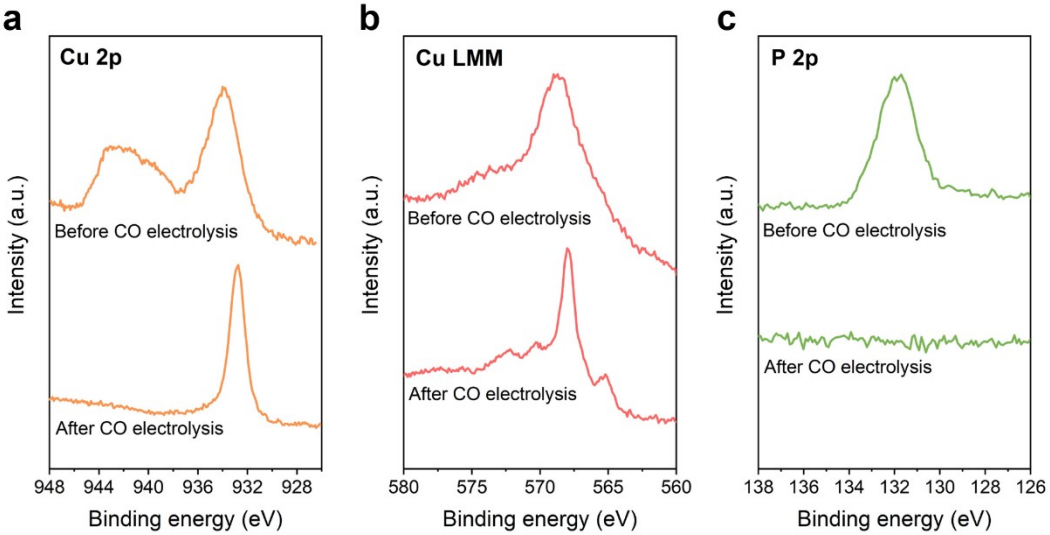

Figure S14. (a) Cu 2p, (b) Cu LMM Auger, and (c) P 2p XPS spectra of the reconstructed $Cu_4P_2O_9$ before and after CO electrolysis.

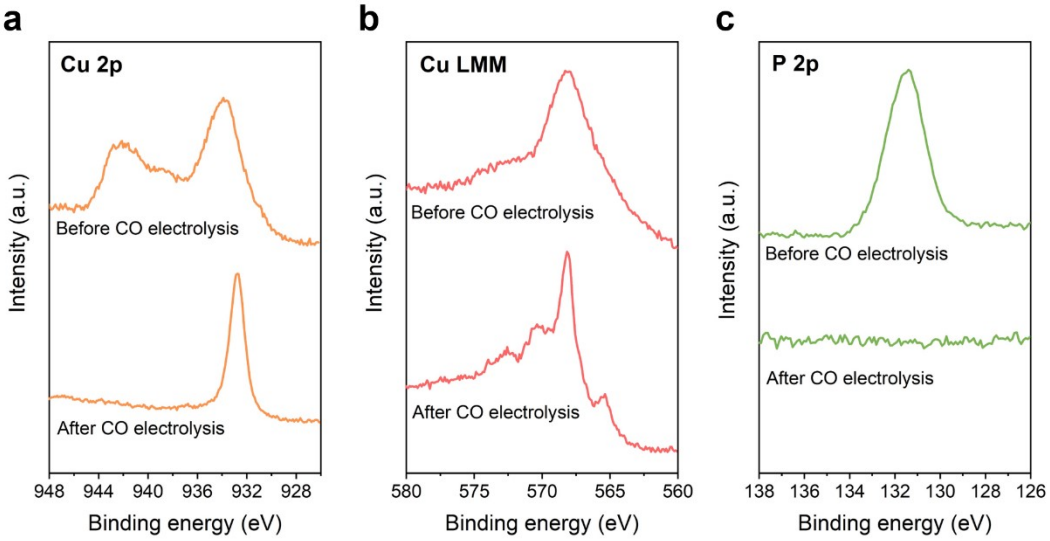

Figure S15. (a) Cu 2p, (b) Cu LMM Auger, and (c) P 2p XPS spectra of the reconstructed $Cu_2P_2O_7$ before and after CO electrolysis.

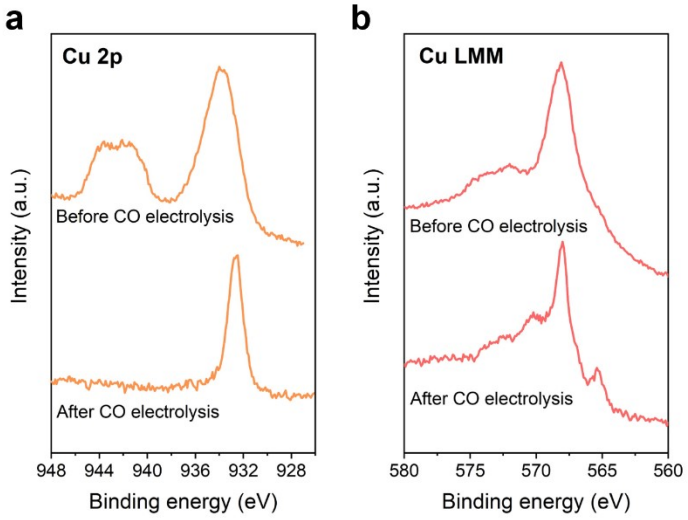

Figure S16. (a) Cu 2p and (b) Cu LMM Auger XPS spectra of CuO before and after CO electrolysis.

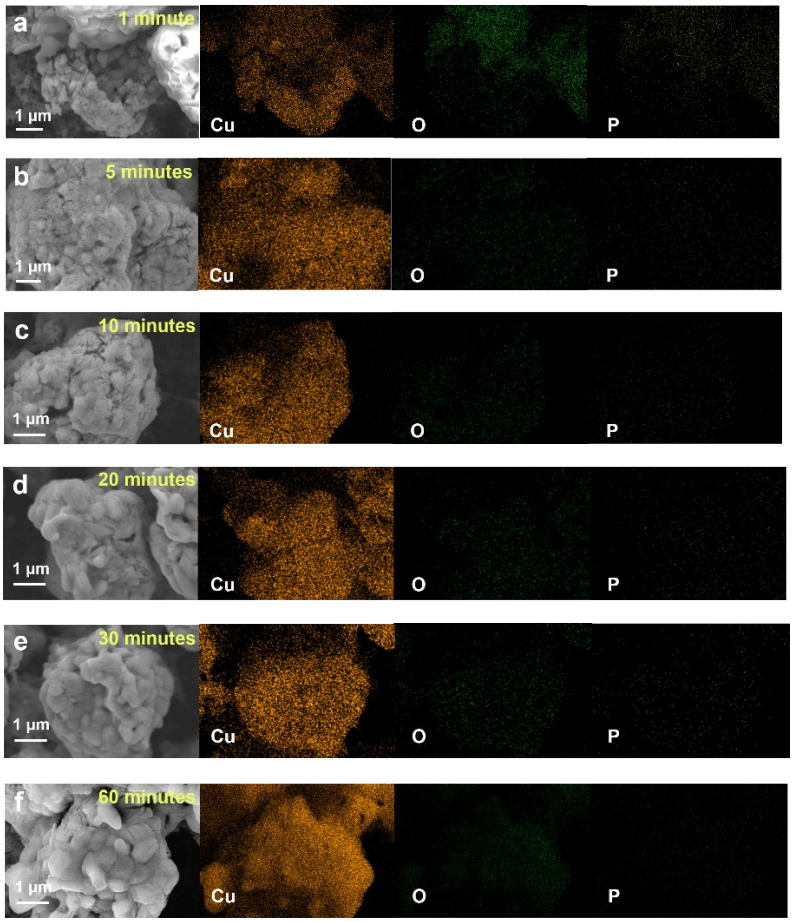

Figure S17. (a–f) SEM image and EDS elemental maps of the reconstructed $Cu_5P_2O_{10}$ catalyst after CO electrolysis for 1–60 minutes.

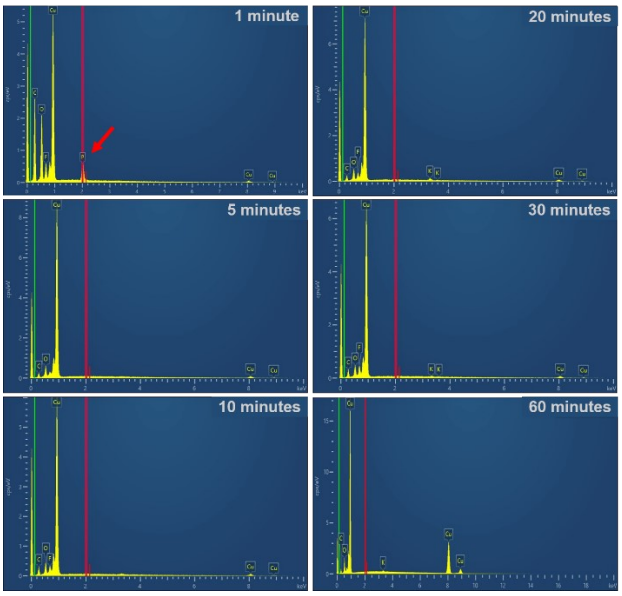

Figure S18. EDS results of reconstructed $Cu_5P_2O_{10}$ catalyst after CO electrolysis for 1–60 minutes. Red line referred to the energy of P.

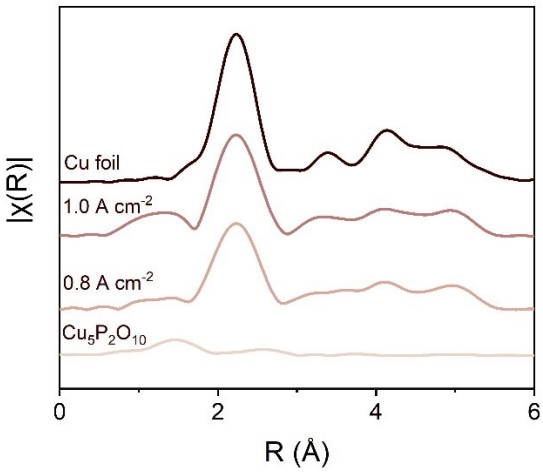

Figure S19. Operando Cu K-edge Fourier-transformed EXAFS spectra of the reconstructed $Cu_5P_2O_{10}$ catalyst at various applied current densities, with Cu foil as reference.

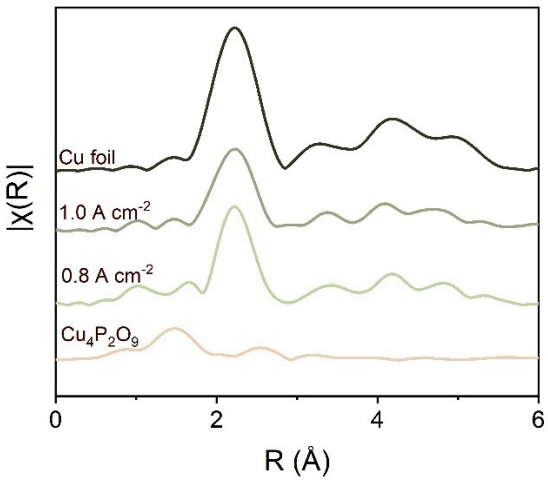

Figure S20. Operando Cu K-edge Fourier-transformed EXAFS spectra of the reconstructed $Cu_4P_2O_9$ catalyst at various applied current densities, with Cu foil as reference.

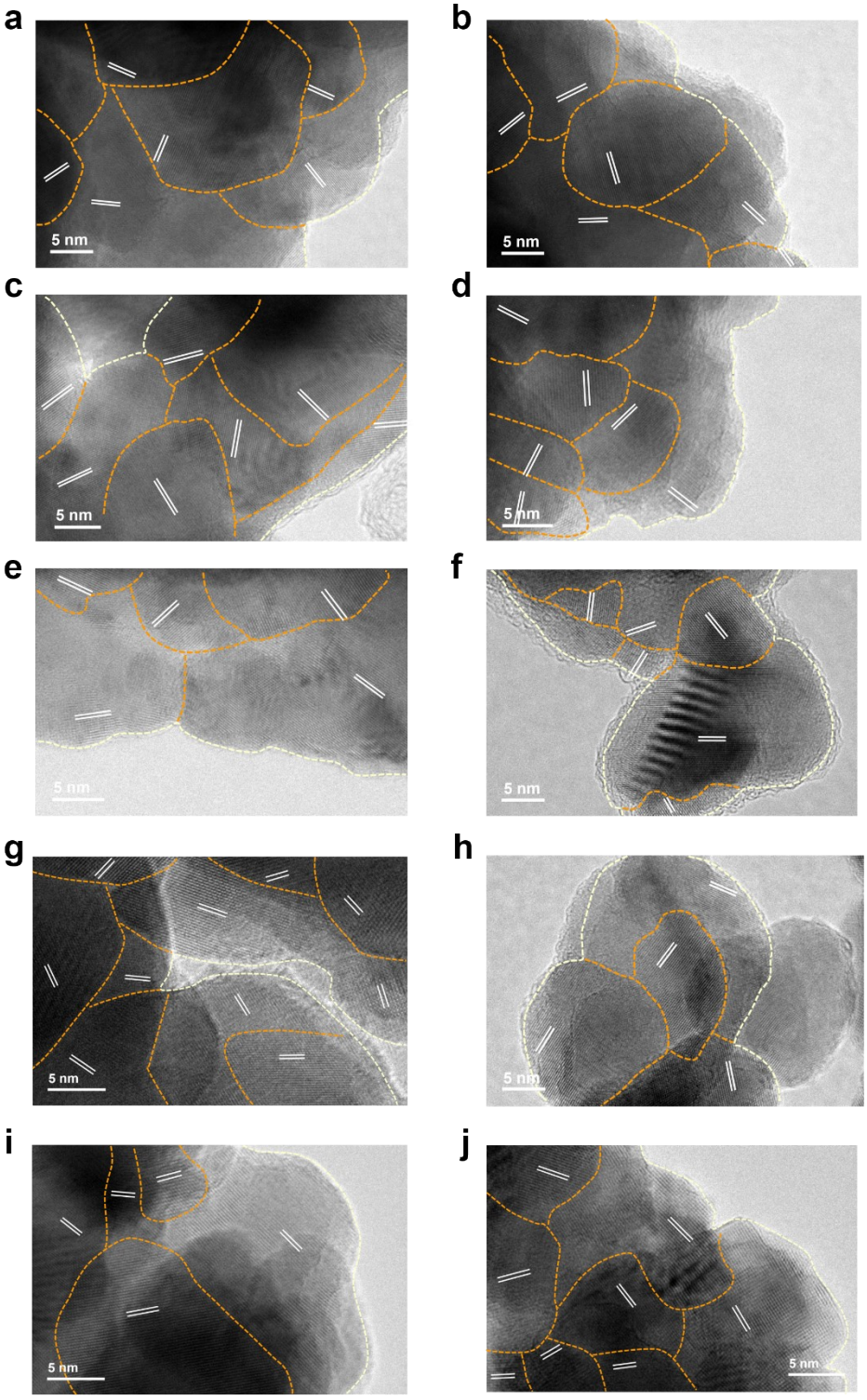

Figure S21. (a–f) HRTEM images of the reconstructed $Cu_5P_2O_{10}$ catalyst after CO electrolysis.

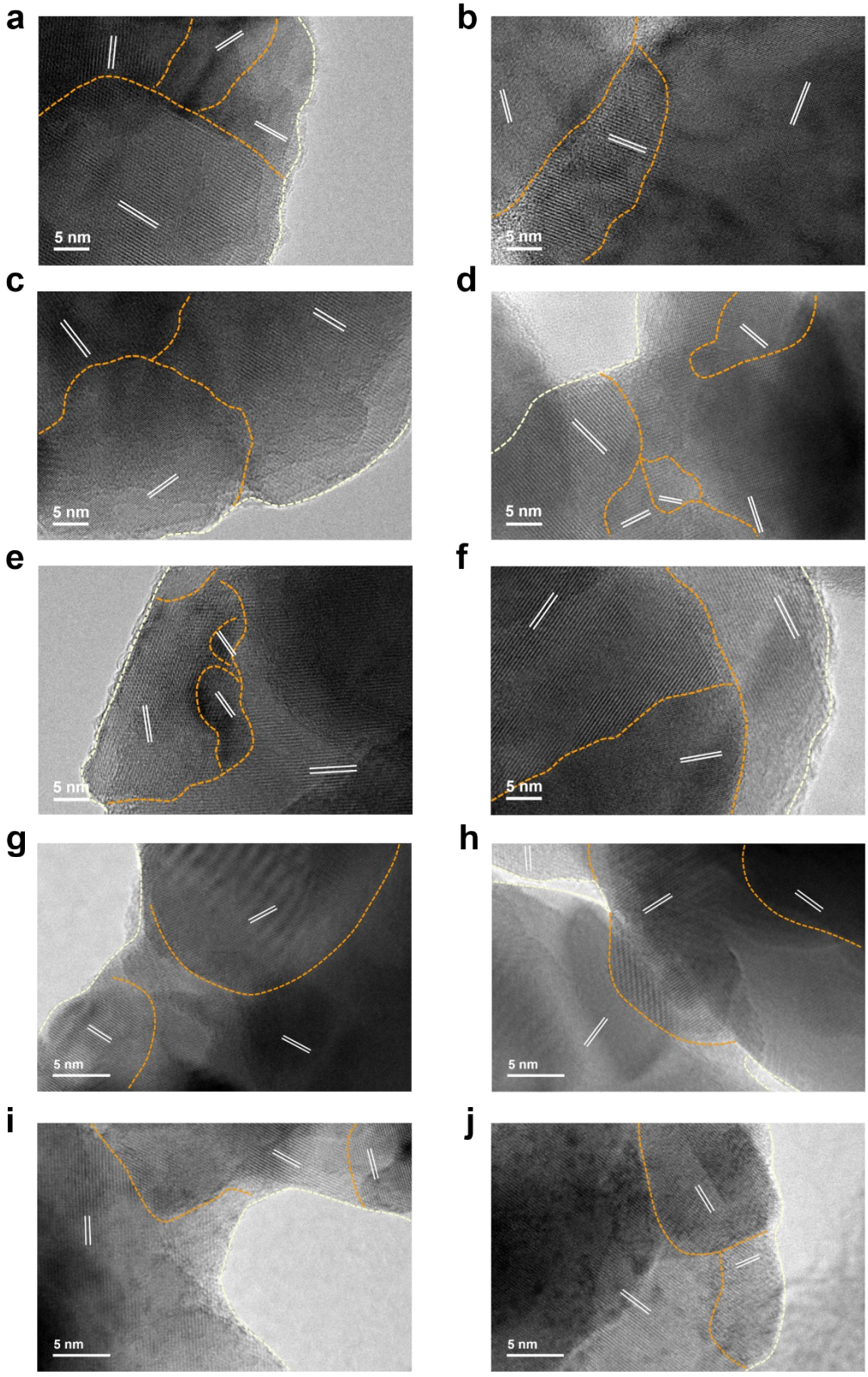

Figure S22. (a–f) HRTEM images of the reconstructed $Cu_4P_2O_9$ catalyst after CO electrolysis.

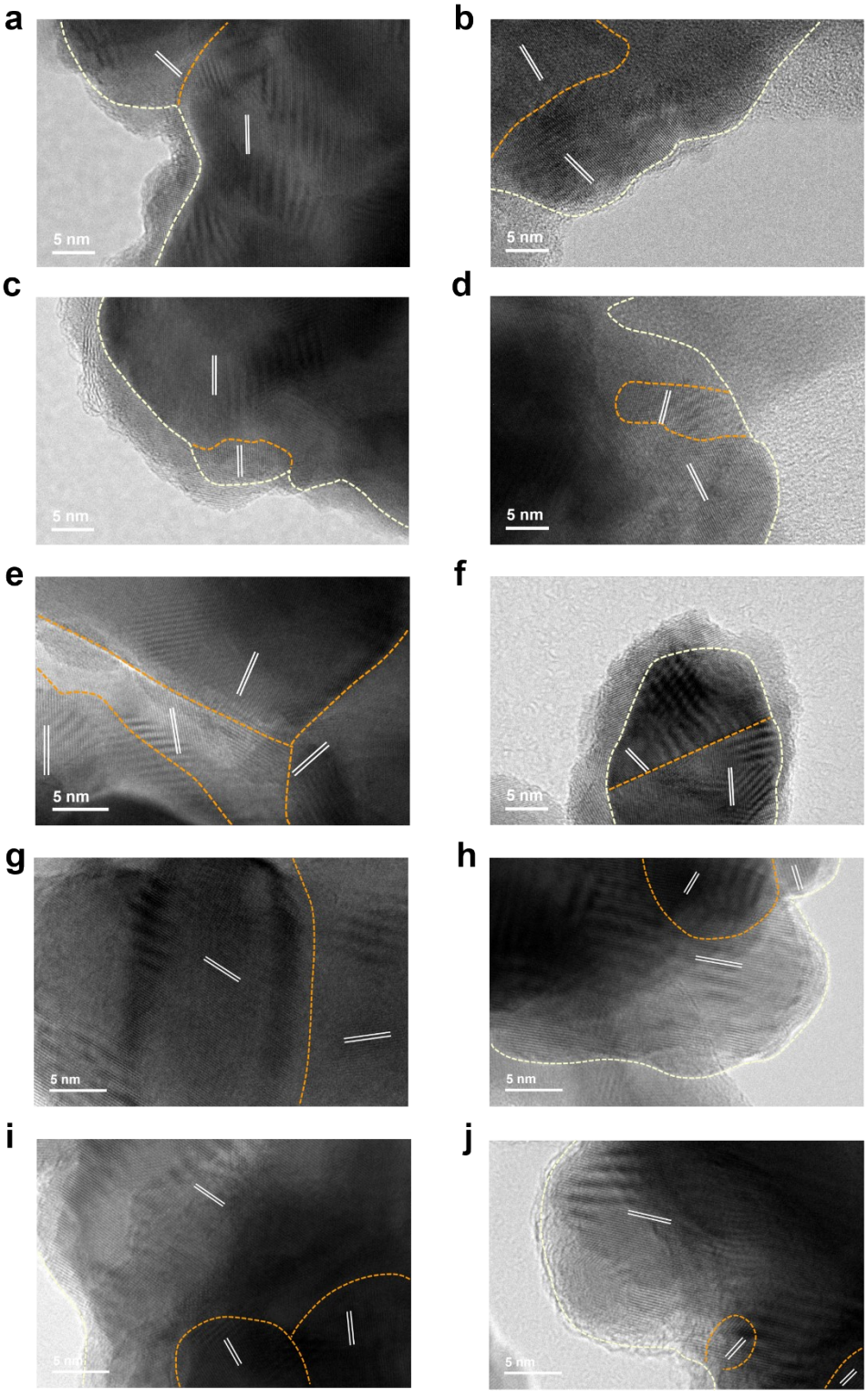

Figure S23. (a–f) HRTEM images of the reconstructed $Cu_2P_2O_7$ catalyst after CO electrolysis.

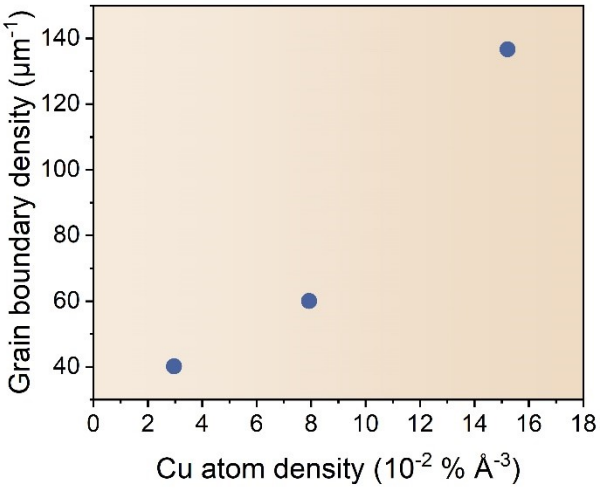

Figure S24. Correlations between surface density of grain boundary generation after CO electrolysis and Cu atom density of as-synthesized $Cu_xP_2O_{x+5}$ catalysts.

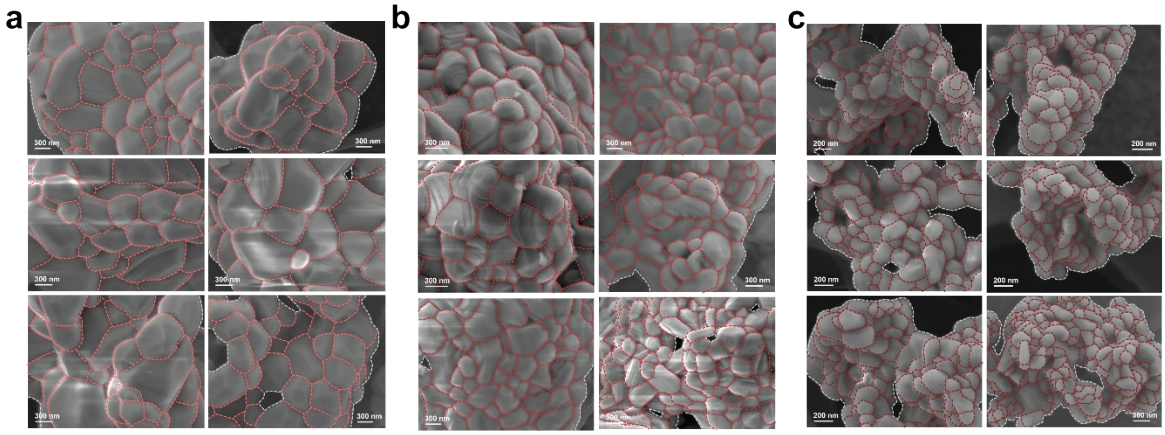

Figure S25. SEM images of (a) $Cu_5P_2O_{10}$, (b) $Cu_4P_2O_9$, and (c) $Cu_2P_2O_7$ catalysts before CO electrolysis.

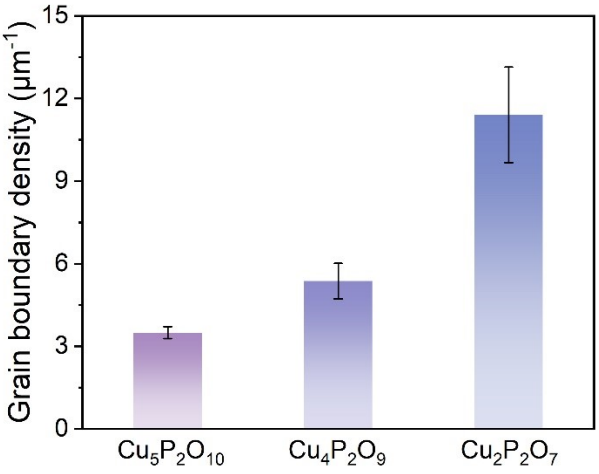

Figure S26. Grain boundary surface density of the $Cu_xP_2O_{x+5}$ catalysts before CO electrolysis.

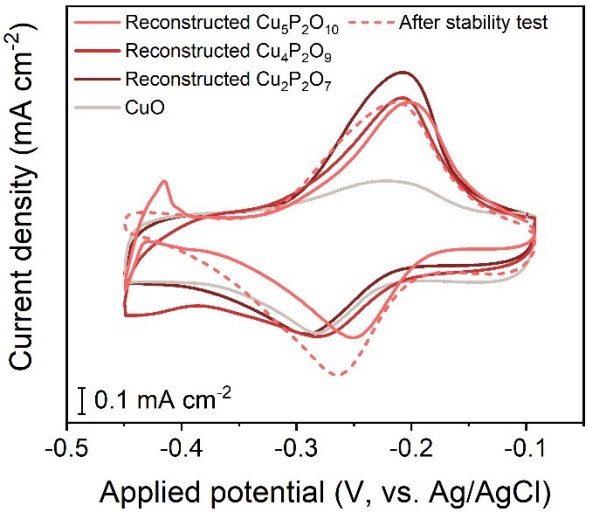

Figure S27. Cyclic voltammograms of Pb underpotential deposition at a scan rate of 10 mV s^{-1} on the reconstructed $Cu_xP_2O_{x+5}$ and CuO catalysts after CO electrolysis.

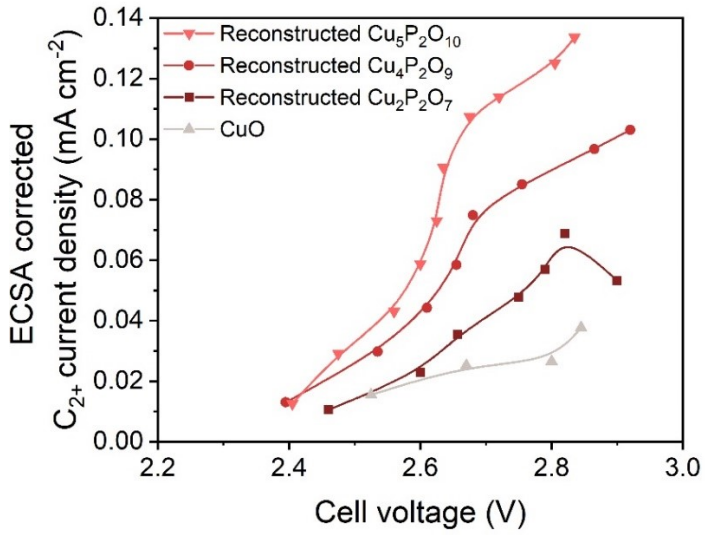

Figure S28. ECSA-corrected current densities for C_{2+} products over the reconstructed $Cu_xP_2O_{x+5}$ and CuO catalysts.

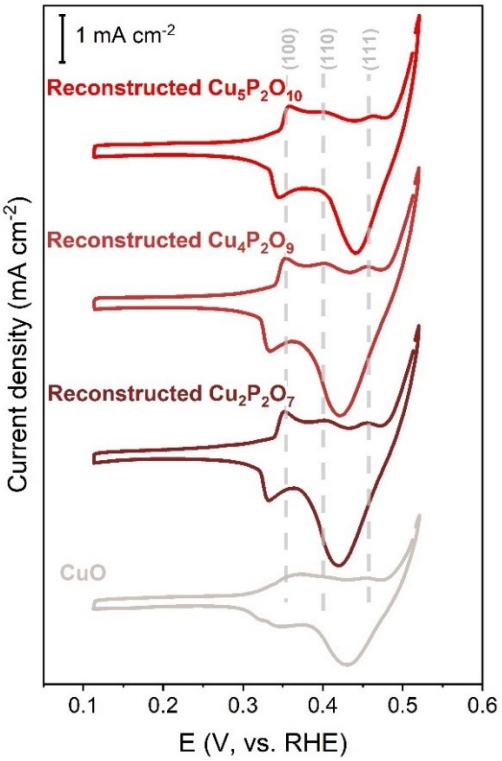

Figure S29. CV curves of the reconstructed $Cu_xP_2O_{x+5}$ and CuO catalysts in Ar-purged 1.0 M KOH. Scan rate: 10 mV s^{-1}.

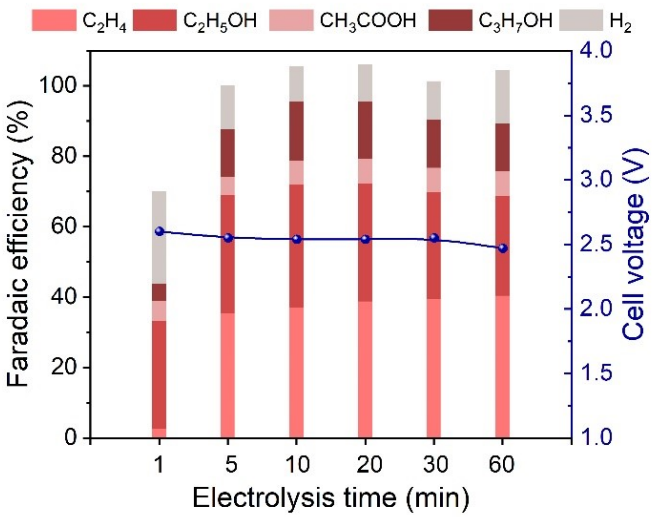

Figure S30. Faradaic efficiencies and cell voltage of the reconstructed $Cu_5P_2O_{10}$ catalysts after CO electrolysis for 1–60 minutes at current density of 0.5 A cm^{-2}.

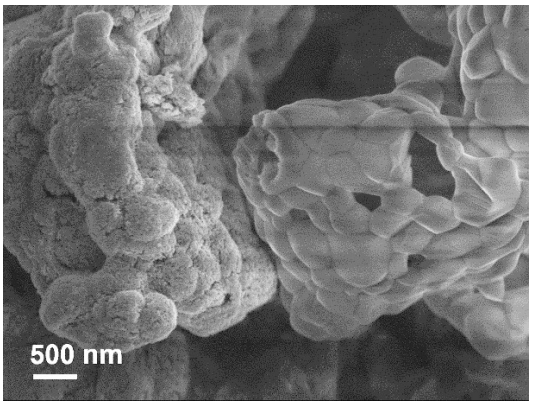

Figure S31. SEM image of reconstructed $Cu_5P_2O_{10}$ catalyst after CO electrolysis for 1 minute. Particle on the right in SEM image is identified as unreacted $Cu_5P_2O_{10}$ precursor.

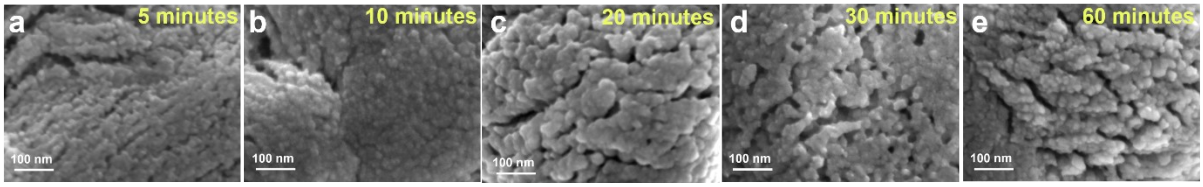

Figure S32. (a–e) SEM images of reconstructed $Cu_5P_2O_{10}$ catalyst after CO electrolysis for 5–60 minutes.

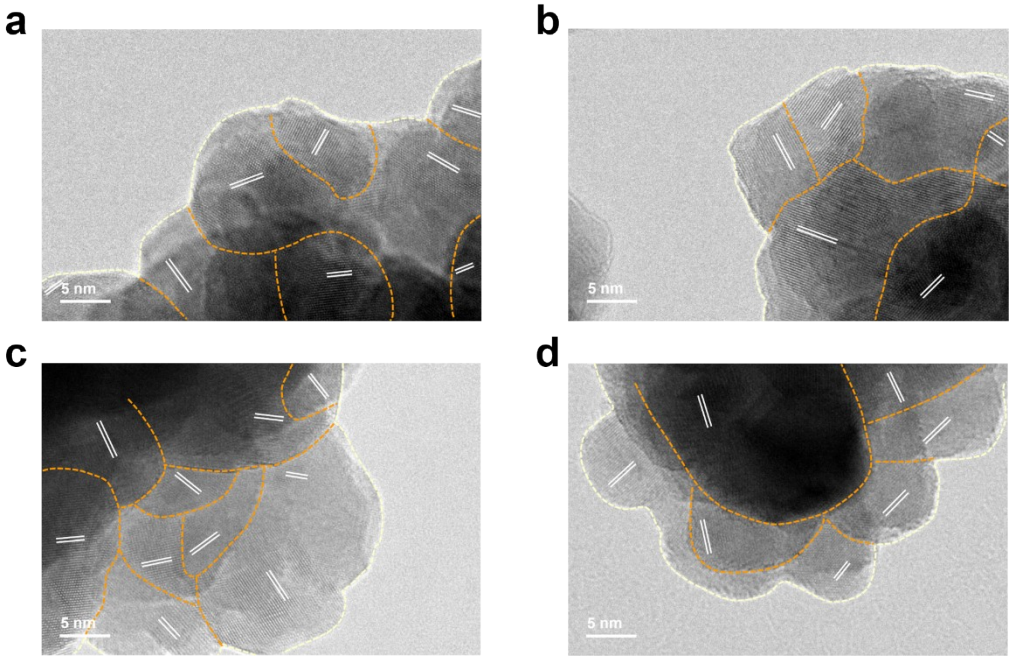

Figure S33. (a–d) HRTEM images of the reconstructed $Cu_5P_2O_{10}$ catalyst after CO electrolysis for 10 minutes.

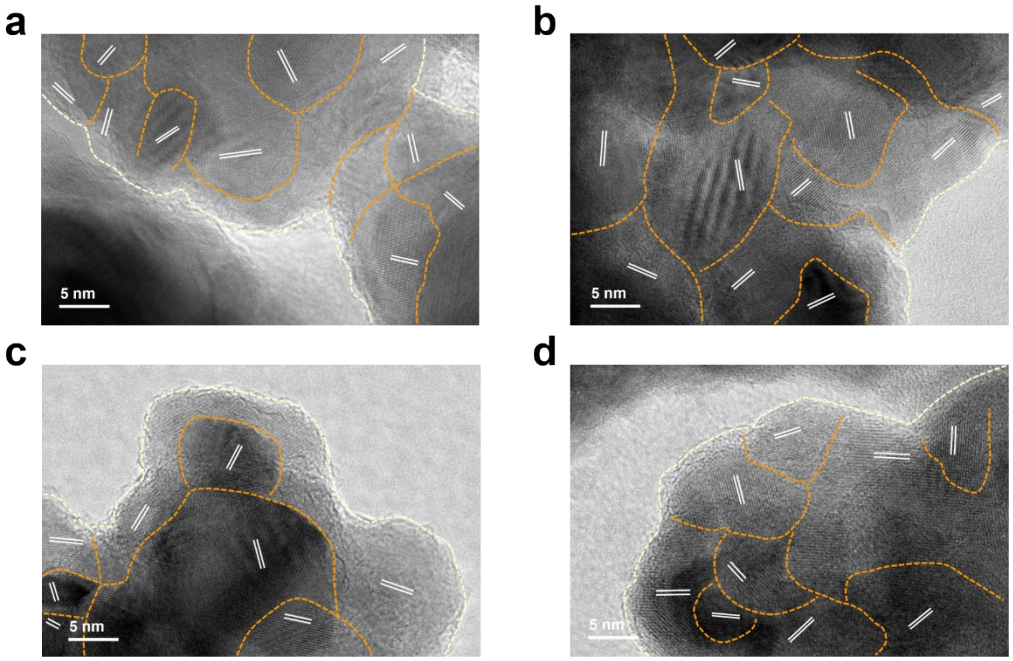

Figure S34. (a–d) HRTEM images of the reconstructed $Cu_5P_2O_{10}$ catalyst after CO electrolysis for 30 minutes.

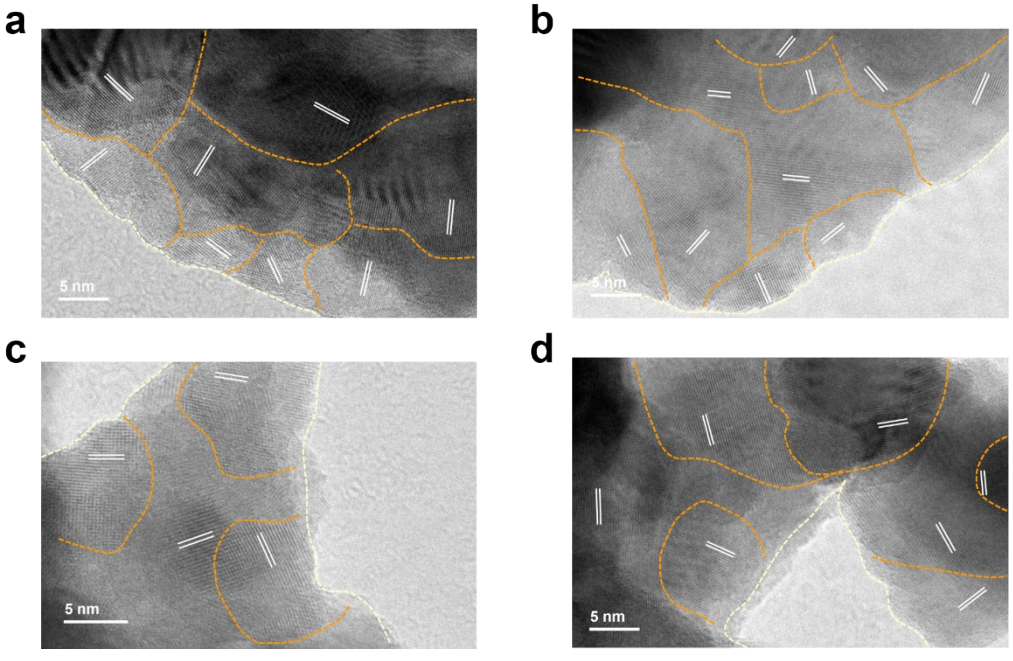

Figure S35. (a–d) HRTEM images of the reconstructed $Cu_5P_2O_{10}$ catalyst after CO electrolysis for 60 minutes.

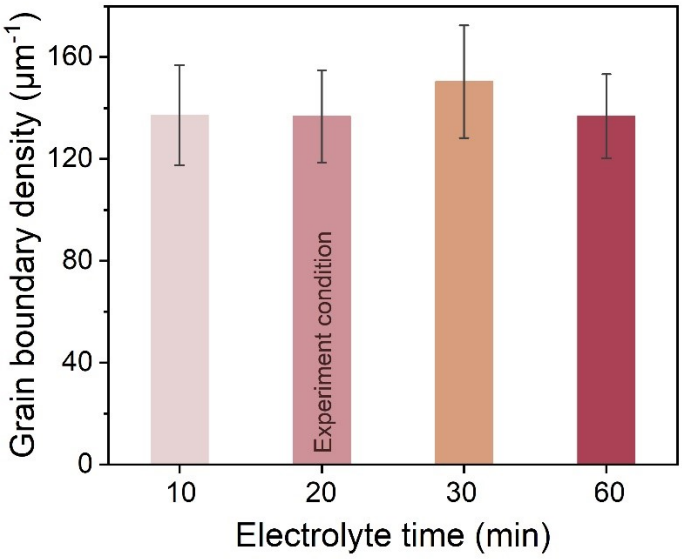

Figure S36. Grain boundary surface density of the reconstructed $Cu_5P_2O_{10}$ catalysts after CO electrolysis for 10–60 minutes.

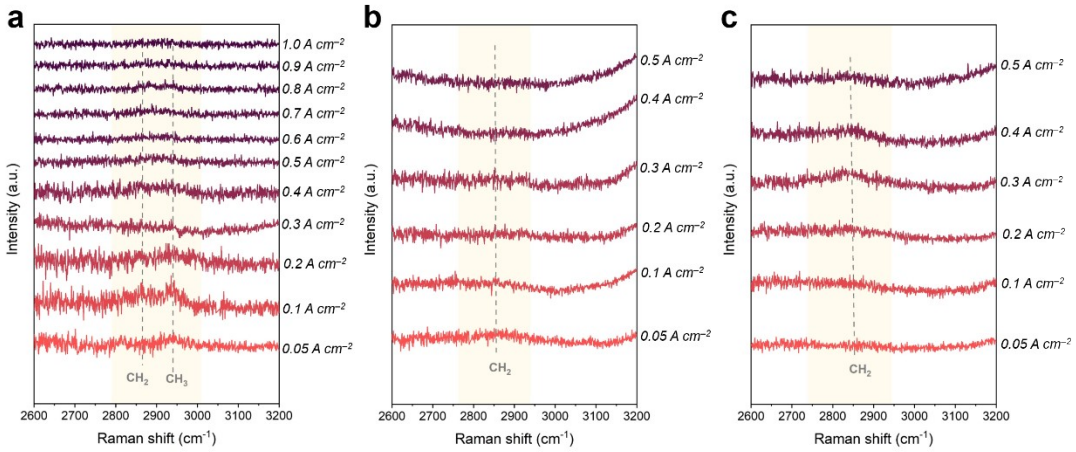

Figure S37. Operando Raman spectra of reconstructed $Cu_xP_2O_{x+5}$ catalysts at different current densities under CO electrolysis condition. Adsorbate region with Raman shift in 2600–3200 cm^{-1} of the reconstructed (a) $Cu_5P_2O_{10}$, (b) $Cu_4P_2O_9$, and (c) $Cu_2P_2O_7$ catalysts.

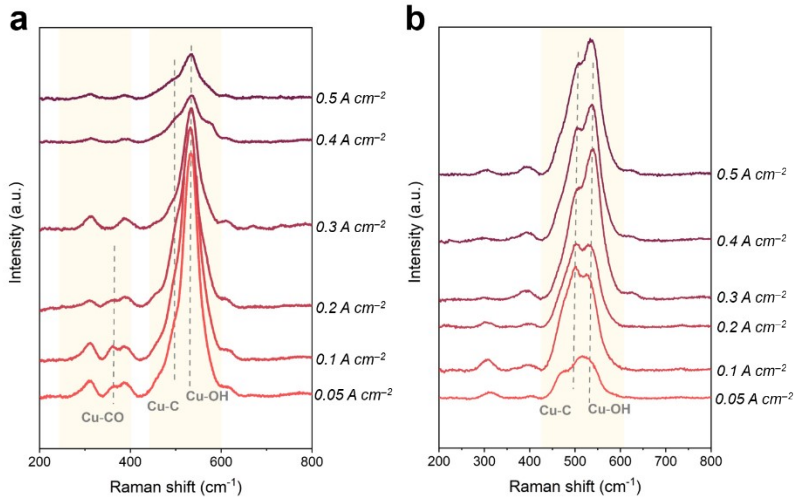

Figure S38. Operando Raman spectra of reconstructed $Cu_xP_2O_{x+5}$ catalysts at different current densities under CO electrolysis condition. Metal-adsorbate region with Raman shift in 200–800 cm^{-1} of the reconstructed (a) $Cu_4P_2O_9$ and (b) $Cu_2P_2O_7$ catalysts.

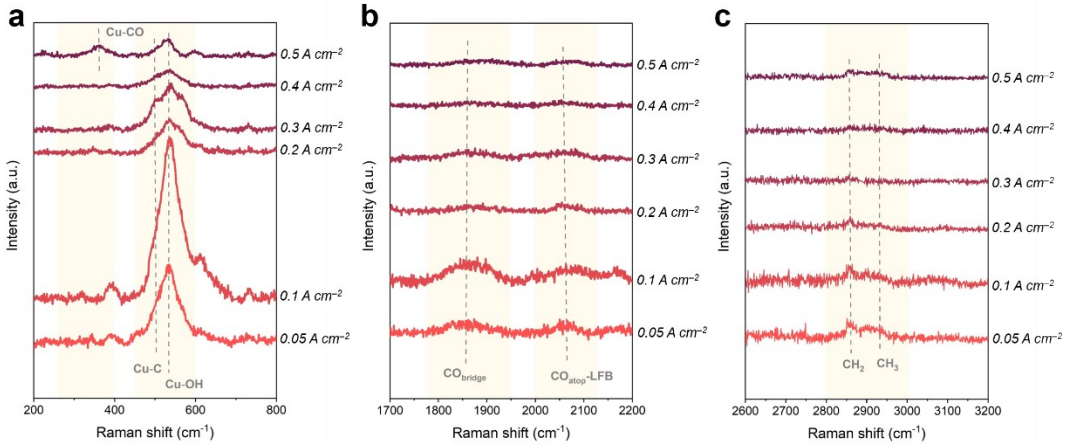

Figure S39. Operando Raman spectra of CuO catalysts at different current densities under CO electrolysis condition. (a) Metal-adsorbate and (b, c) adsorbate regions.

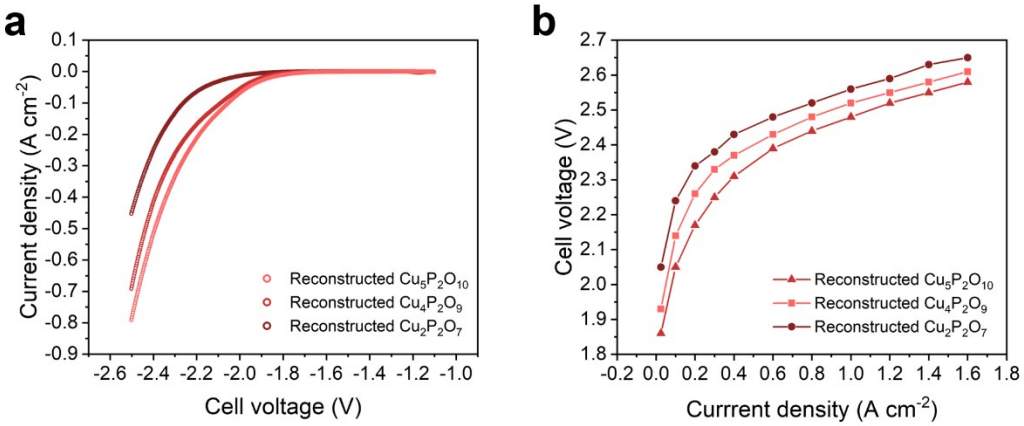

Figure S40. (a) LSV curves and (b) current density-cell voltage curves measured in Ar flow in MEA-based electrolyzer after CO electrolysis.

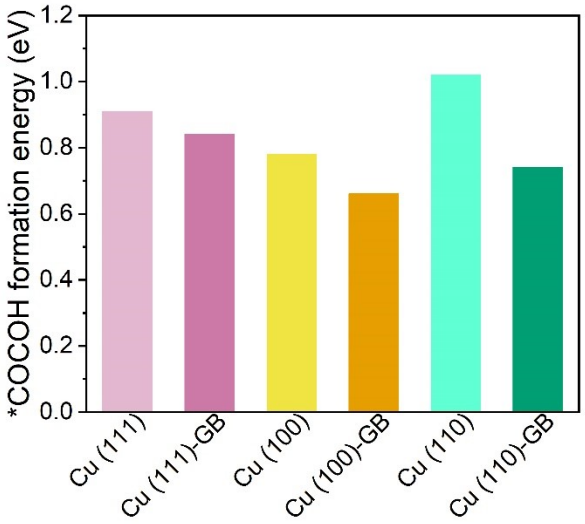

Figure S41. The *COCOH formation energy on Cu surface and corresponding grain boundaries.

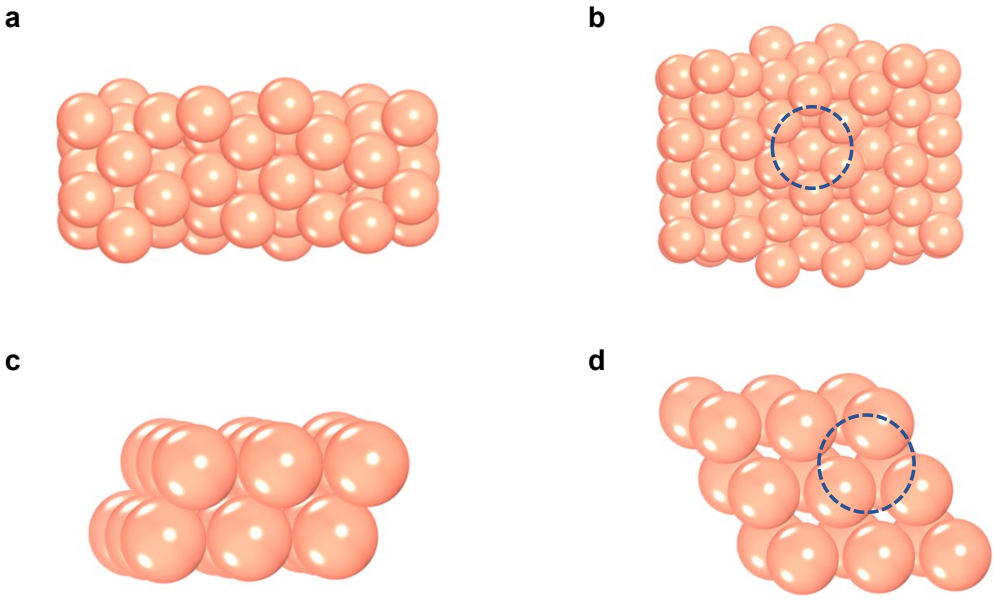

Figure S42. The grain boundary model and Cu (111) model with (a), (c) side view and (b), (d) top view. The active site area used for DFT calculations is enclosed by blue dashed lines. For clarity, only the two topmost layers are shown in Cu (111) model.

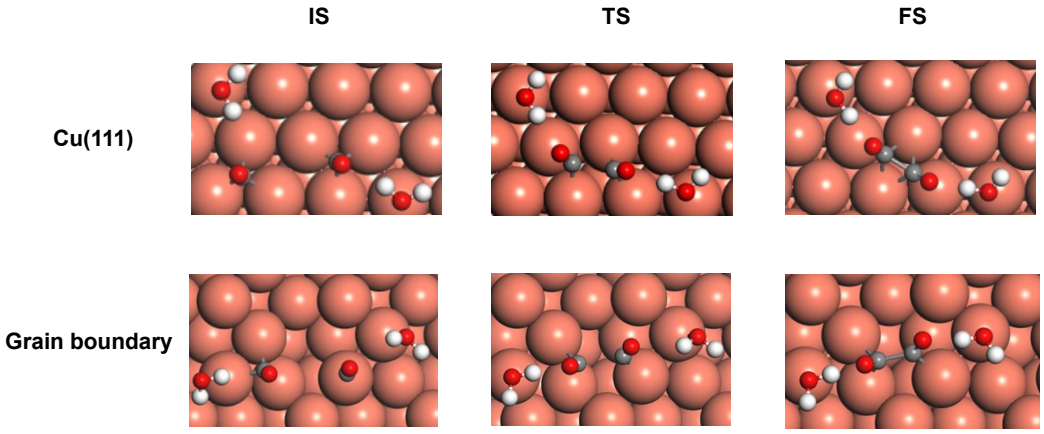

Figure S43. The initial state (IS), transition state (TS) and final state (FS) for *CO−*CO coupling on Cu (111) and grain boundary site.

Table S1. Distribution of Cu, P and O atom, cell volume and Cu atom density in unit cell of $Cu_xP_2O_{x+5}$.

Catalyst	Crystal cell atomicity of Cu	Crystal cell atomicity of P	Crystal cell atomicity of O	Ratio of Cu crystal cell atomicity (%)	Cell volume ($Å^3$)	Cu atom density (10^{-2} % $Å^{-3}$)
$Cu_2P_2O_7$	6	8	28	14.29	482.6	2.960
$Cu_4P_2O_9$	8	4	18	26.67	336.3	7.929
$Cu_5P_2O_{10}$	5	2	10	29.41	193.3	15.22

Table S2. Surface area of $Cu_xP_2O_{x+5}$ catalysts before CO electrolysis.

Catalyst	BET surface area (m^2 g^{-1})	V_{total} (cc g^{-1})
$Cu_5P_2O_{10}$	0.85	6.100E-3
$Cu_4P_2O_9$	1.12	9.560E-3
$Cu_2P_2O_7$	0.90	8.785E-3

Table S3. Comparison of CO electrolysis performance towards C_{2+} products at industrial current density.

Catalyst	C_{2+} FE (%)	j_{C2+} (A cm^{-2})	Electrolyte	Potential	Reference
Cu nanosheet	~70	0.21	2 M KOH	~–0.74 V vs. RHE	15
OD-Cu	91	0.63	1 M KOH	~–0.66 V vs. RHE	16
Cu:py:SSC	85	0.136	3 M KOH	2.5 V (Full cell voltage)	17
OD Cu	>90	1.125	1 M KOH	–0.72 V vs. RHE	18
Cu-HDD	>90	0.654	1 M KOH	–0.74 V vs. RHE	19
CuPd	95	0.576	1 M KOH	–1.03 V vs. RHE	12
CuAgO	91.7	0.504	1 M $CsHCO_3$	~–0.87 V vs. RHE	20
Cu/Cu_2O	93.5	0.150	2 M KOH	–0.70 V vs. RHE	21
$Cu(OD)_{0.8}Ag_{0.2}$	90.2	~0.135	1 M KOH	–0.56 V vs. RHE	22
CuO nanosheet	88	1.05	0.1 M KOH	2.98 V (Full cell voltage)	23
Reconstructed $Cu_5P_2O_{10}$	93.3	1.306	0.1 M KOH	2.67 V (Full cell voltage)	This work
Reconstructed $Cu_5P_2O_{10}$	85.1	1.702	0.1 M KOH	2.81 V (Full cell voltage)	This work

Table S4. ICP-OES analysis of P element in the flow out electrolyte during CO electrolysis over $Cu_5P_2O_{10}$ catalyst.

Electrolyte time	Sample Concentration Units (mg/L)	Standard deviation
1 minute	62.73	0.361
5 minutes	3.682	0.0379
10 minutes	2.012	0.0511
20 minutes	0.064	0.0179
30 minutes	N.D.[a]	-
60 minutes	N.D.	-

[a]N.D.-not detected

Table S5. Statistical results of grain boundary surface density of the reconstructed $Cu_xP_2O_{x+5}$ catalysts.

Catalyst	Mean corrected surface density of grain boundary (μm^{-1})	Standard deviation
Reconstructed $Cu_5P_2O_{10}$	136.6	18.1
Reconstructed $Cu_4P_2O_9$	60.0	11.8
Reconstructed $Cu_2P_2O_7$	40.1	15.3

Table S6. Statistical results of grain boundary surface density of the $Cu_xP_2O_{x+5}$ catalysts before CO electrolysis.

Catalyst	Mean corrected surface density of grain boundary (μm^{-1})	Standard deviation
$Cu_5P_2O_{10}$	3.5	0.22
$Cu_4P_2O_9$	5.4	0.65
$Cu_2P_2O_7$	11.4	1.7

Table S7. The measured Pb stripping charge and roughness factor for different electrodes.

Electrode	Pb stripping charge ($\mu C\ cm^{-2}$)	Roughness factor
Reconstructed $Cu_5P_2O_{10}$	4193	12.73
Reconstructed $Cu_5P_2O_{10}$ after stability test	4548	13.81
Reconstructed $Cu_4P_2O_9$	4261	12.94
Reconstructed $Cu_2P_2O_7$	5122	15.55
CuO	1366	4.15

Table S8. Statistical results of grain boundary surface density of the reconstructed $Cu_5P_2O_{10}$ catalysts after CO electrolysis for 10–60 minutes.

Electrolysis time (min)	Mean corrected surface density of grain boundary (μm^{-1})	Standard deviation
10	137.2	19.6
20	136.6	18.1
30	150.3	22.1
60	136.8	16.5

Table S9. Standard enthalpy change (ΔH_i^0) and thermoneutral voltage (E^n) for CO electrolysis.

Net reaction	ΔH_i^0 (kJ mol^{-1})	E^n (V)
$2CO + 2H_2O \rightarrow C_2H_4 + 2O_2$	845	1.094
$2CO + 3H_2O \rightarrow C_2H_5OH + 2O_2$	801	1.038
$2CO + 2H_2O \rightarrow CH_3COOH + O_2$	308.2	0.8
$3CO + 4H_2O \rightarrow C_3H_7OH + 3O_2$	1170.35	1.01

Reference

1. P. Wei, H. Li, L. Lin, D. Gao, X. Zhang, H. Gong, G. Qing, R. Cai, G. Wang and X. Bao, *Sci. China Chem.,* 2020, **63**, 1711-1715.
2. J. Li, K. Chang, H. Zhang, M. He, W. A. Goddard, J. G. Chen, M.-J. Cheng and Q. Lu, *ACS catal.*, 2019, **9**, 4709-4718.
3. G. Kresse and J. Furthmüller, *Comput. Mater. Sci.*, 1996, **6**, 15-50.
4. G. Kresse and J. Furthmüller, *Phys. Rev. B*, 1996, **54**, 11169-11186.
5. B. Hammer, L. B. Hansen and J. K. Nørskov, *Phys. Rev. B*, 1999, **59**, 7413-7421.
6. Y. Zhang and W. Yang, *Phys. Rev. Lett.*, 1998, **80**, 890-890.
7. P. E. Blöchl, *Phys. Rev. B*, 1994, **50**, 17953-17979.
8. G. Kresse and D. Joubert, *Phys. Rev. B*, 1999, **59**, 1758-1775.

9. S. Grimme, *J. Comput. Chem.*, 2006, **27**, 1787-1799.
10. J. Cheng, J. Luo and K. Yang, *Comput. Mater. Sci.*, 2018, **155**, 92-103.
11. A. A. Peterson, F. Abild-Pedersen, F. Studt, J. Rossmeisl and J. K. Nørskov, *Energy Environ. Sci.*, 2010, **3**, 1311-1315.
12. Y. Ji, Z. Chen, R. Wei, C. Yang, Y. Wang, J. Xu, H. Zhang, A. Guan, J. Chen, T.-K. Sham, J. Luo, Y. Yang, X. Xu and G. Zheng, *Nat. Catal.*, 2022, **5**, 251-258.
13. Y. Xie, P. Ou, X. Wang, Z. Xu, Y. C. Li, Z. Wang, J. E. Huang, J. Wicks, C. McCallum, N. Wang, Y. Wang, T. Chen, B. T. W. Lo, D. Sinton, J. C. Yu, Y. Wang and E. H. Sargent, *Nat. Catal.*, 2022, **5**, 564-570.
14. H. Xiao, T. Cheng, W. A. Goddard, III and R. Sundararaman, *J. Am. Chem. Soc.*, 2016, **138**, 483-486.
15. W. Luc, X. Fu, J. Shi, J.-J. Lv, M. Jouny, B. H. Ko, Y. Xu, Q. Tu, X. Hu, J. Wu, Q. Yue, Y. Liu, F. Jiao and Y. Kang, *Nat. Catal.*, 2019, **2**, 423-430.
16. M. Jouny, W. Luc and F. Jiao, *Nat. Catal.*, 2018, **1**, 748-755.
17. A. Ozden, Y. Wang, F. Li, M. Luo, J. Sisler, A. Thevenon, A. Rosas-Hernández, T. Burdyny, Y. Lum, H. Yadegari, T. Agapie, J. C. Peters, E. H. Sargent and D. Sinton, *Joule*, 2021, **5**, 706-719.
18. J. Li, Z. Wang, C. McCallum, Y. Xu, F. Li, Y. Wang, C. M. Gabardo, C.-T. Dinh, T.-T. Zhuang, L. Wang, J. Y. Howe, Y. Ren, E. H. Sargent and D. Sinton, *Nat. Catal.*, 2019, **2**, 1124-1131.
19. C. Zhao, G. Luo, X. Liu, W. Zhang, Z. Li, Q. Xu, Q. Zhang, H. Wang, D. Li, F. Zhou, Y. Qu, X. Han, Z. Zhu, G. Wu, J. Wang, J. Zhu, T. Yao, Y. Li, H. J. M. Bouwmeester and Y. Wu, *Adv. Mater.*, 2020, **32**, 2002382.
20. N. Martić, C. Reller, C. Macauley, M. Löffler, A. M. Reichert, T. Reichbauer, K.-M. Vetter, B. Schmid, D. McLaughlin, P. Leidinger, D. Reinisch, C. Vogl, K. J. J. Mayrhofer, I. Katsounaros and G. Schmid, *Energy Environ. Sci.*, 2020, **13**, 2993-3006.
21. G. Ma, O. A. Syzgantseva, Y. Huang, D. Stoian, J. Zhang, S. Yang, W. Luo, M. Jiang, S. Li, C. Chen, M. A. Syzgantseva, S. Yan, N. Chen, L. Peng, J. Li and B. Han, *Nat. Commun.*, 2023, **14**, 501.
22. J. Li, H. Xiong, X. Liu, D. Wu, D. Su, B. Xu and Q. Lu, *Nat. Commun.*, 2023, **14**, 698.
23. P. Wei, D. Gao, T. Liu, H. Li, J. Sang, C. Wang, R. Cai, G. Wang and X. Bao, *Nat. Nanotechnol.*, 2023, **18**, 299-306.